Tribology International 179 (2023) 108126

Contents lists available at ScienceDirect

Tribology International

journal homepage: www.elsevier.com/locate/triboint

Combining discrete and continuum mechanics to investigate local wear processes induced by an abrasive particle flow

A. Quacquarelli [a,*], G. Mollon [a], T. Commeau [b], N. Fillot [a]

[a] Univ Lyon, INSA Lyon, CNRS, LaMCoS, UMR5259, 69621 Villeurbanne, France
[b] Umicore Specialty Powders France, 38100 Grenoble, France

ARTICLE INFO

Keywords:
Abrasive wear
Damage
Cohesive zone model

ABSTRACT

Wear caused by hard debris or abrasive slurries trapped between moving surfaces is a major industrial problem concerning engineering and agriculture machine components, causing abrasion and reducing their service life. In this context, the wear of diamond tools used to cut stones represents an interesting case study due to the particular tribological interactions involved. Diamond tools are characterised by diamonds (the cutting edge) and the metal matrix (the retaining binder). While several attempts have been made to analyse diamond wear, the wear process involving the matrix is not yet well understood. In particular, the phenomena responsible for wear at the local scale have not yet been fully investigated as they are difficult to quantify experimentally and the existing numerical models, to the authors' knowledge, greatly simplify the physical behaviour and interactions between the different materials in contact. A new code is therefore used in this work. It is able to treat the metal matrix as a deformable polycrystalline material and the debris flow by controlling the shape and size of the grains. Furthermore, the wear of the metal matrix will be described as a loss of intergranular cohesion caused by the continuous passage of debris through a cohesive contact law that also takes fatigue into account. The model will show, albeit qualitatively, that the wear of the metal surface is caused by the asperities of the debris grains, thus validating one of the fundamental assumptions behind the model defined by the same authors at a larger scale. Another aspect investigated is the relationship between the temporal evolution of wear and the roughness of the metal surface. Again, it will be shown how the temporal evolution of the metal surface is consistent with what has been observed in the literature. Moreover, due to the complexity of the model, a sensitivity study will be necessary to understand the physical significance of the parameters and how to adapt them to the specific case study. It will then be shown how these parameters can change the physics of the problem being analysed and must therefore be chosen carefully.

1. Introduction

Wear caused by hard debris or abrasive slurries trapped between moving surfaces is a major industrial problem concerning engineering and agriculture machine components, causing abrasion and reducing their service life [1–3].

Although wear is a broad common problem, it remains a fairly complex issue because it is not a property of the material but rather the response of the system under certain contact conditions [4]. A useful conceptual tool in understanding wear phenomena is the tribological triplet firstly proposed by Godet and Berthier [5]: abrasive particles define the third body of the tribosystem, i.e., the interface material that can result from the degradation of the two bodies in contact -the first bodies- (hard grains in cutting operations, fine airborne grit particles in lubricating oil) or from the outside (hard particles in agriculture or mining operations).

Whatever the cause of wear, some mechanical transformation and physical/chemical phenomena occur at the contacting surface, demonstrating that wear is a complex phenomenon where all features involved are strongly related and cannot be studied separately. In particular, the third body may be more or less heterogeneous and continuous; its thickness may vary in a wide range of values (from a few nanometers to several micrometers), is characterized by unknown rheology [6] and its abrasive power depends on some physical properties such as hardness [1], grain size [7–10] and angularity [11–14]. In this context, this work deals with the wear of diamond tools used in rock cutting. Diamond

* Corresponding author.
E-mail address: quacquarelli.adriana@gmail.com (A. Quacquarelli).

https://doi.org/10.1016/j.triboint.2022.108126
Received 20 September 2022; Received in revised form 18 November 2022; Accepted 24 November 2022
Available online 26 November 2022
0301-679X/

tools include core drills and saw blades (Fig. 1a.) and are composed of abrasive segments fixed to steel core by brazing or welding. Segments consist of diamond crystals embedded into a metallic matrix by a sintering process (Fig. 1b.). During the cutting operations, pressure is applied to the core to guarantee a constant feed velocity and is fully transferred to the diamonds and then to the rock to cut it. The matrix retains the diamonds, which, due to their hardness, are able to indent the workpiece. Debris particles from the cut material are inevitably formed, defining, together with the water used to carry them out, a slurry. This slurry, in turn, constitutes an abrasive debris flow able to wear the matrix. This wear process, illustrated in Fig. 1c., is necessary to renew diamonds, meaning that wear is not always deleterious, but should be nevertheless controlled in terms of wear rate: the matrix has to wear to a rate compatible with the diamond breakdown to attain an optimum between the service life and the free cutting ability. For these reasons, the wear resistance of the matrix has to be adjusted to the wear speed of the diamond: if the matrix is too soft, it wears fast, and the diamond capacity is not completely used with a premature diamond pull-out; if it wears more slowly than diamonds, then the slurry cannot be carried out correctly, and the segment will continuously lose the ability to cut.

Bearing in mind that diamond tool wear affects both the diamonds and the matrix surface, this work does not cover diamond breakage and essentially deals with the abrasive wear of the matrix surface, which in turn depends on several aspects such as [15]:

- The type of rock: marble, granite, concrete, and reinforced concrete behave differently during processing [16] and generate debris particles different in shape, size, and hardness, therefore with different abrasive powers.
- Segment specifications: the number and surface of segments (scale of the tool), the diamonds distribution and concentration (scale of the segment), and the matrix material and microstructural properties (scale of the matrix) affect the cutting process and the rate of wear. Cobalt-based alloys are commonly used to produce matrices for diamond tools for their high abrasive resistance and great retention properties [17].
- Operational parameters: feed rate, peripheral speed, force applied, and cooling efficiency (i.e. coolant type and flow rate) [18] define the cutting tool. In particular, the processed rock and the coolant used, exert control on the rheological properties of the slurry.

The importance of diamonds on (metal) matrix wear is clear when observing a segment of a diamond tool after a cutting operation. For circular saws and core drills (Fig. 1a.) where the direction of the cutting velocity is constant, the degradation of the metal surface takes the form defined in Fig. 2 with a crater behind each diamond and a tail in front of it [19].

Several studies have been done to analyse, at least qualitatively, the wear of the surface in terms of reduction of the diamond retention after the manufacturing process [20–22] and in working conditions [23], while mechanisms involved in the matrix wear are not yet well understood. Studies performed under optical and electronic microscopes allow the analysis of metal matrix wear in relation to diamond wear [24,25], while [26] observed that abrasive wear is the predominant mode in cutting tools.

It was also experimentally observed that, in the optimum cutting conditions, the workpiece wears away faster than the metallic surface, such that particles detached from the workpiece are present in a much larger quantity than detached particles from the matrix (generally stuck to debris grains, as illustrated in Fig. 3).

This aspect can be better understood and quantified by referring to the tribological circuit, i.e., a useful conceptual tool initially proposed by Berthier [5] and then reformulated by Fillot and co-workers to represent better the wear of a degradable material by discrete elements modelling [27]. In the general case where both contacting surfaces are degradable materials (Fig. 4a.), detached particles define the internal source flow Q_s, while particles detached from the system defines the ejection flow Q_e. Defining wear no longer as the loss of mass from one material but the loss of mass from the whole contact [5], the wear flow $Q_w$is the amount of ejected particles that definitely leave the system, while the remaining part defines the recirculation flow Q_r and is reintroduced in the system (Fig. 4b.).

In the specific case of diamond tools, after the diamond indentation into the workpiece, debris grains from the workpiece are continuously renewed during the cutting process, such that each ejected particle is immediately replaced by new ones and by the recirculation flow. This means that a steady state is reached fast and the total mass of the third body inside the contact remains almost constant [28]. This evidence allows defining the mass of the third body as being characterized only by grains of debris. Moreover, there is a constant recirculation of debris grains, meaning that the amount of particles detached from the workpiece is equal to the particles ejected and the debris flow mass is almost constant. This equilibrium is also guaranteed by the tail formed behind each diamond giving the right support (Fig. 2). For these reasons, the wear of the matrix does not depend on the metallic grains themselves but is only due to the slurry.

The tribological circuit is an essential aid in understanding wear by bridging the gap between experimental observations and numerical modelling. The advantage of running numerical simulation is the possibility of understanding mechanisms that cannot be observed experimentally and of predicting the wear behaviour (under certain well-defined conditions) without undergoing experimental tests, thereby reducing development costs. However, this latter objective can be achieved only after the model has been validated with known experimental results. A numerical wear model to predict wear at the scale of the industrial application has been developed by the same authors as in the present work in [29]. This model considers the wear of the matrix surface during a drilling operation; it takes into account the characteristics of the slurry both in terms of flow and rheology and at a more local level by considering the size and shape of the debris with particular regard to asperities. These aspects are then implemented in a wear law that takes the form of Archard's law. This model is therefore well suited to predict wear on a macroscopic scale representing the wear around one single diamond as already defined looking at Fig. 2. However, it is not able to describe the more local phenomena that are not even experimentally accessible at the scale of the industrial process (i.e., the grains detachment and ejection from the matrix caused by the continuous circulation of debris rock). For this reason, the following model is intended as a complementary study to the experimental campaign [24,25] and the model presented in [29]. The purpose is to offer a numerical tool dealing with the phenomenological understanding of the abrasive wear process referring to the scale of the contact between the abrasive grains and the surface being worn. At this scale, continuous models do not seem to be very suitable. Meanwhile, great progress has been made in recent decades in the area of Discrete Element Modelling (DEM) developed by Cundall and Strack in 1979 in the field of geomaterials [30] and then extended to a wide scientific domain going from granular mechanics to civil and mechanical engineering. In particular, in the tribology community, this approach was used by Iordanoff and co-workers [31] to analyze the effect of cohesion on third body particles both in two and three-dimension. Then, Fillot and co-workers implemented the degradation of the first body into the discrete element establishing an early phenomenological wear model [27]. This model provides a sound basis for understanding wear. However, to better represent physics, it is necessary to go further than just representing materials as a collection of rigid spheres, accounting for aspects such as the abrasiveness of hard particles and the microstructure of the degradable first bodies. Mollon [32] introduced a 3D model based on the Voronoi tessellation in the DEM framework to account for the roughness and degradation of a surface subjected to frictional contact. For the model to be used for damage and wear studies, it is necessary to implement more realistic contact laws. The current trend consists of coupling discrete methods

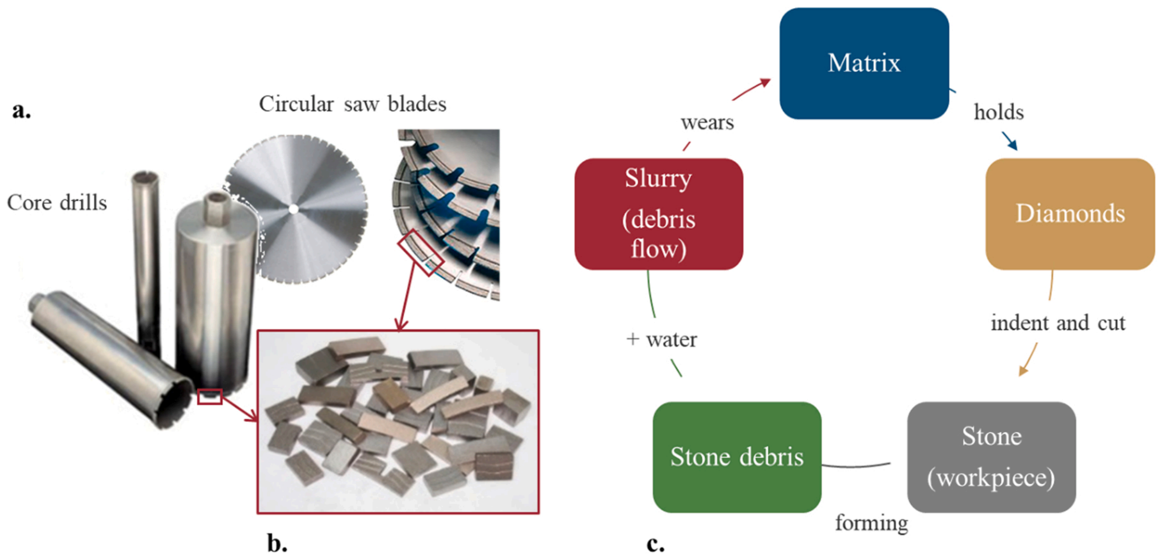

Fig. 1. Definition of diamond tools: **a.** Core drill and circular saw blades; **b.** cutting segments; **c.** Cutting and wear process.

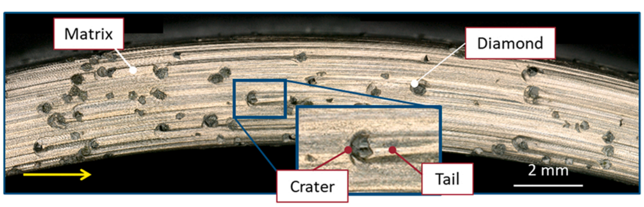

Fig. 2. Segment surface observed by the optical microscope after a drilling operation. Insert: zoom on one diamond and the wear around it with the indication of the debris flow direction in yellow (kindly granted by USPF[11]).

with finite elements to describe mainly the dynamics of the third body while the first bodies are modelled as continua by finite elements. One of the main limitations of FEM is that the stress and strain fields representations are strictly related to the triangles of the mesh (or tetrahedrons in 3D) presenting some mesh-related distortion issues. On the other hand, meshfree methods are a valid alternative offering a more realistic and accurate representation, guaranteeing continuous stress and strain fields independently on the mesh [33]. In this framework, the meshless multibody method is a hybrid technique between FEM and DEM. It can account for a large number of particles, both rigid and deformable, and of any shape and size distribution, overcoming the main difficulties of the finite element approach. The multibody technique was implemented by Mollon [34,35] in the MELODY_2D code (Multibody ELement-free Open code for DYnamic simulation) and applied in several tribological situations [36–38].

In the present study, through the MELODY_2D code, wear is defined as a function of stress cycles induced by the continuous passage of rock debris and intergranular loss of cohesion of the matrix. The discrete approach allows representing the matrix microstructure as a degradable and deformable polycrystalline material in which grains are held together by cohesion, and the slurry as a collection of hard grains with controlled shapes and sizes. The originality of this work lies in taking into account the many different aspects involved in the wear process entirely in their complexity. This type of modelling clearly requires considerable numerical effort. Starting from the case study already described, we will first detail the modelling choices (Section 2), continuing with an analysis of the results in Section 3. Some conclusions and perspectives are then outlined in Section 4.

2. Numerical framework

2.1. Numerical modeling of wear

To understand and describe wear mechanisms that are not accessible at the scale of experiments, this model looks at a representative element of the matrix microstructure in contact with the debris flow, as illustrated in Fig. 5a. Notably, the matrix microstructure is designed by sintering cobalt powders with micro-diamonds (Fig. 2). This cobalt powder is generally controlled in grain size and porosity since these two

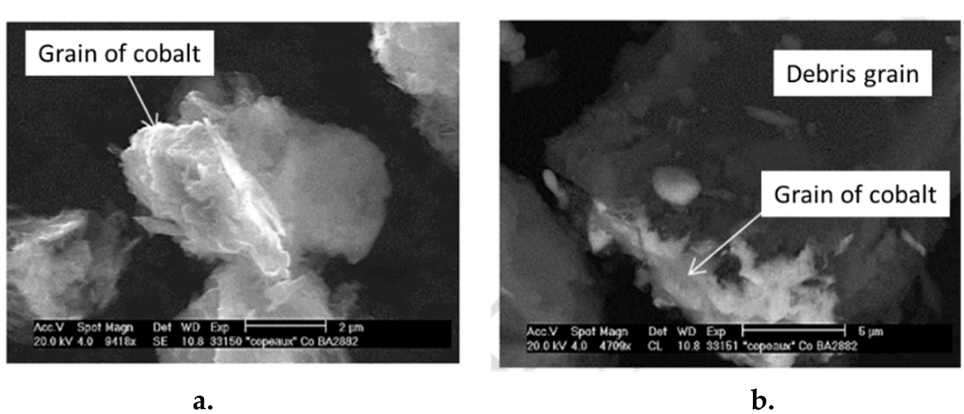

Fig. 3. a. SEM image of a cobalt grain; b. SEM image of a debris grain with a gain of cobalt stuck to it [25].

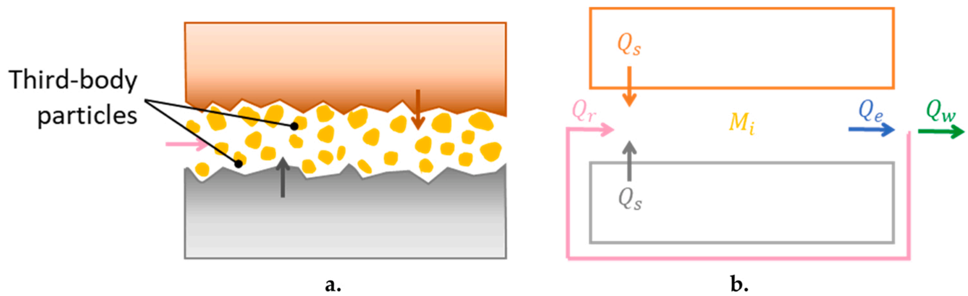

Fig. 4. a. The schematization of the tribological triplet with the definition of the first bodies and the third body; b. the schematization of the tribological circuit: Q_s: source flow; Q_e: ejection flow; Q_r: recirculation flow; Q_w; : third-body mass (from[27]).

properties affect the mechanical behaviour of the material [39,40]. To account for its polycrystalline nature, the matrix microstructure is numerically described as a collection of deformable grains (see Section 2.2) prolonged by a deformable non-degradable base of the same material on the top (Fig. 5b-d). The matrix dimensions must be appropriately chosen to avoid any perturbations at the boundary and guarantee continuity between the degradable and the non-degradable part since there is no intended mechanical discontinuity between them. It is straightforward that the larger the degradable thickness, the larger the number of grains modelled and the costlier the simulation is. Therefore, the continuum substrate is necessary to limit the simulation cost by reducing the thickness of the degradable part, while avoiding the effect of a rigid boundary on the stress fields. Based on this required continuity between the two parts, the height of the degradable and non-degradable matrix are respectively chosen as $h_m = 20\mu m$ and $h_b = 30\mu m$. The matrix microstructure is also in contact with rock debris grains which define the third body of the system; they are modelled as rigid grains with irregular shapes (see Section 2.2) and occupy an initial thickness (before compaction) $h_{debris} = 50\mu m$; and are in turn in contact with the workpiece, modeled as a rigid continuum body of the same material as the debris flow. In this way, wear is defined as the matrix grains detachment and ejection from the system, caused by the continuous passage of rock debris, as explained in the Introduction.

The length of the domain $L_x$is set one order of magnitude larger than the thickness of the degradable matrix h_m ($L_x = 200\mu m$) to ensure the respect of periodic boundary conditions on the lateral sides of the system (necessary to the modeling of the continuous debris flow recirculation) and avoid boundary effects while optimizing the computation time. The boundary conditions must be correctly chosen to represent any portion of the matrix in contact with the debris flow without taking into account the presence of diamonds. The upper side of the continuum microstructure is fixed, while the workpiece is subjected to normal pressure and a sliding velocity (Fig. 5b.), like in a cutting operation. The normal pressure is taken equal to the average one applied by the machine to each segment. In practice, this pressure is almost entirely taken up by the diamonds to indent the rock; however, for the sake of simplicity, it is assumed here that it is equally distributed over the segment. Future studies could consider the hydrodynamic pressure exerted by the debris particles calculated through the Reynolds equation [41] at a macroscale [29]. The sliding velocity is taken one order of magnitude higher than the one generally used in the cutting operation. As will be explained in Section 3.1, this choice is necessary to accelerate the simulation and does not impact the debris flow regime, which remains in the range of dense granular flows [42]. Fig. 5 also shows in detail the main sub-domains that characterize the system. As will be better illustrated below, the continuum metallic base as well as the metal matrix grains are handled as deformable bodies and thus require additional field nodes for their representation (Fig. 5c–d).

It is worth noting that, by definition, in a meshfree model, the discretization is only required to define the density of field nodes and its possible gradient but does not include any strict connectivity relation between them, as described in [35]. The smaller typical nodal distance is set to $d_{nodes} = 0.1\mu m$. Debris grains are rigid bodies so only boundary nodes are needed for their definition.

2.2. Materials characterization and grains generation

Both matrix and debris grains, whose main features are listed in Table 1, are generated numerically and packed by targeting their shape and size using the code PACKING2D [43].

Concerning the matrix microstructure, the powder microstructure used in this study was designed by USPF (Fig. 6a.). The grains follow a lognormal distribution that is approached by generated packing of grains (Fig. 6b.). The main procedure starts with the domain definition and its discretization into sub-domains using the Voronoi Tesselation as illustrated at the top of Fig. 6c., where each subdomain is occupied by a grain: the size and orientation of grains can be statistically controlled by imposing the size distribution and orientation of corresponding cells. Then, the matrix microstructure is cleaned from acute angles and small edges that may cause instability problems in the contact resolution during the simulation. This procedure allows to add some roughness on the contacting surface with the debris flow (y = 0 in Fig. 6c. bottom). This also leads to an “artificial porosity” (visible in Fig. 6d.) that is purely numerical and remains very limited. Apart from that, the model can approximately reproduce the real size distribution of the microstructure.

Roughness generated numerically may evolve during working conditions. To relate roughness to wear, it is important to define the main roughness parameters, which are the moments of the profile amplitude density function [44]. The moment of first and second order are the mean and the standard deviation respectively (R_a and R_q), while the skewness (third order moment, R_{sk}) and the kurtosis (fourth order moment, R_{ku}) are related to the spatial distribution of the roughness, their meaning is illustrated in Fig. 7 applyied to the particular case study. The initial values of the four moments are listed in Table 2.

Concerning the slurry, debris grains are generated by the cutting of concrete and are generally sub-angular to angular (Fig. 8a.), with 90 % of the population between 1 μm and 100 μm. The size distribution is bimodal with modes of 20 μm and 2 μm, respectively, with a median value of 10 μm (Fig. 8b.). After domain generation and the definition of the Voronoi tessellation, the shape of grains is randomly generated by providing some angularities and facetting to simulate the realistic debris shape (Fig. 8c.). The shape is controlled by the definition of Fourier Descriptors; each of them indicates a shape characteristic, as documented in [43]. Fig. 8b. plots the real and simulated grain size distribution. Since the model is not able to cover the real wide size distribution, the packing is generated by imposing the same median

[1] Umicore Specialty Powder France

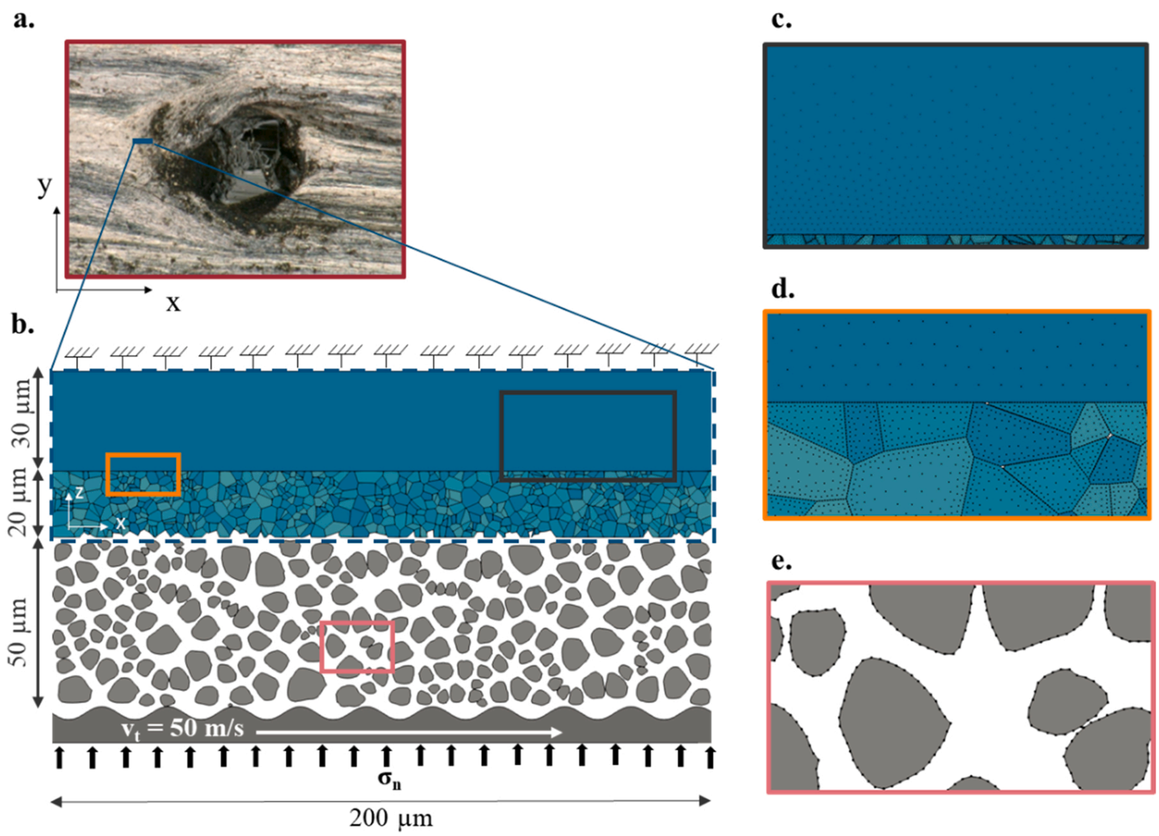

Fig. 5. Definition of the numerical model: **a.** Wear of the matrix around one diamond observed by optical microscopy (kindly granted by USPF); **b.** Sketch of the numerical model with (from top to bottom) a deformable metallic substrate, a deformable and degradable microstructure, a discretized granular rigid third body, and a rigid workpiece; **c.** zoom on the contact with the continuum and degradable metallic surface; **d.** zoom on grains microstructure and definition of the integration points; **e.** zoom on the rigid debris grains.

Table 1
Experimental parameters for matrix and debris during a drilling operation [24].

Debris and Matrix Parameters		
Matrix grain size (before sintering)	2	µm
Matrix grain size (after sintering)	2.3	µm
Porosity of microstructure	18	%
Vickers Hardness	299	HV10
Average rock debris diameter	20	µm

value as the one measured experimentally.

It should be noted that the definition of wear at the macroscopic scale required the rheological characterization of the debris flow; therefore, a rheological characterization of debris grains mixed with water was performed and is described in [29]. For what concerns this study, only the grain size and the shape of debris grains are considered, and rheology spontaneously emerges from their collective behavior.

2.3. Contact laws

In this model, the following contact laws are used:

(a) Mohr-Coulomb: for the contact between debris grains and grains of the degradable microstructure, for the debris grains-workpiece contact, and the contact between debris grains themselves. The coefficient of friction is set to $\mu = 0.3$ which is consistent with values defined in literature for grains-grains contact [45]. Further improvements to the model can also consider the effect of the intergranular friction coefficient on the damage and wear.

(b) Triangular Cohesive zone model (CZM) with fatigue to ensure the continuity between the degradable and the continuous matrix microstructure, but especially to describe the degradation of the metal matrix (caused, in turn, by the continuous passage of rock debris).

The cohesive zone model was initially proposed by Hillerborg and co-workers [46] based on the model proposed by Barenblatt [47] to define fracture in brittle material as a gradual phenomenon. This approach is now generally used to model the fracture of polycrystalline materials. In particular, Dugdale [48] applied a similar model to investigate the yielding and sizing of a crack tip on the plastic zone, while Zhou & Molinari applied the cohesive crack opening process to study the brittle failure in ceramic materials by FEM, introducing a rate-dependent cohesive law [49]. Different studies were performed on fatigue crack growth using a CZM approach. Most of them aimed to analyze the mechanical resistance of materials and the intergranular fracture in the fracture mechanics framework. Only a few such works address tribological situations. Champagne and co-workers [50] performed the implementation of the CZM on the investigation of friction and wear of a biphasic material. Sadeghi and co-workers focused on rolling contact fatigue dealing with microstructural cracks that develop at the scale of contacting surfaces [51].

For what concerns this work, the fatigue CZM is used to model the grain detachment: grains of the microstructure are held together by an inter-granular cohesion which is progressively reduced by the pressure and velocity exerted by the debris flow. This loss of cohesion opens a gap between grains, both in the normal and tangential direction, as illustrated in Fig. 9a. for two grains taken from the matrix defined in Fig. 6c. The crack interface separation in the tensile direction δ_n (mode I) and in

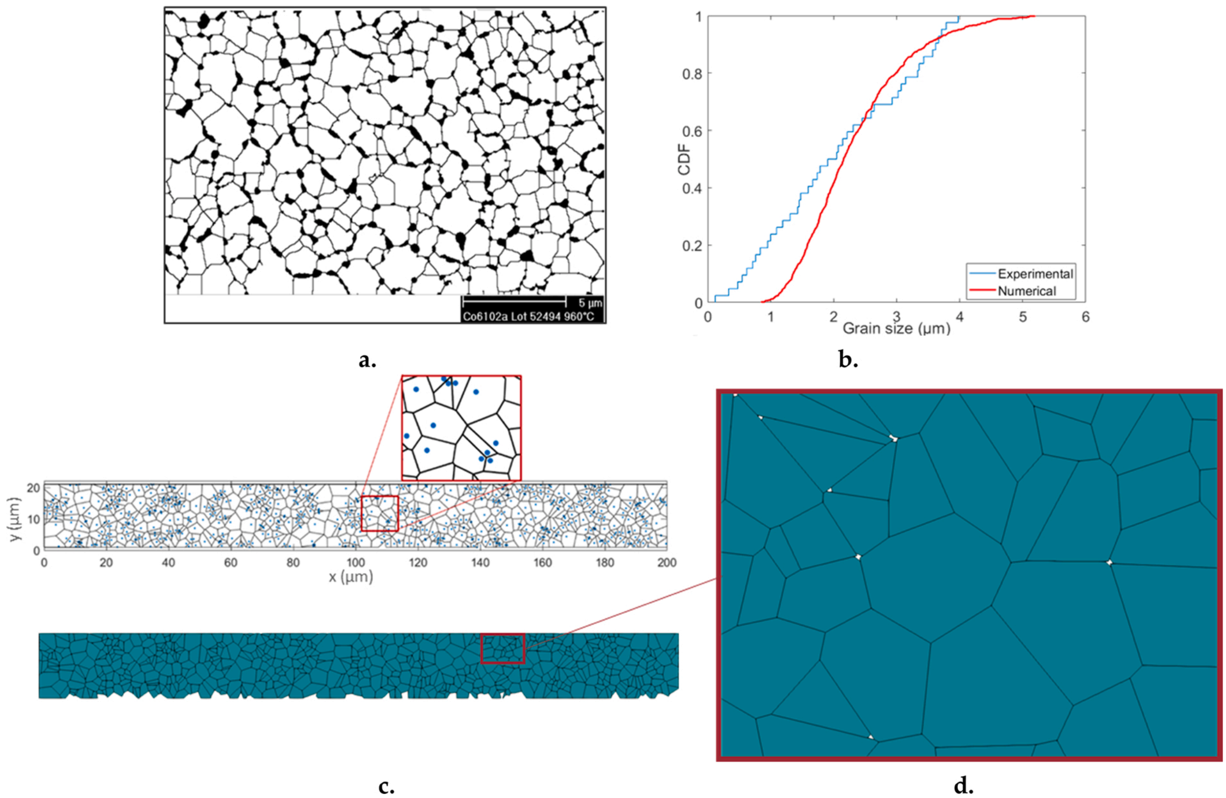

Fig. 6. Definition of the matrix microstructure: **a.** cobalt matrix microstructure observed by SEM (black zones are the porosity of the microstructure) [24] **b.** comparison between the experimental and numerical grain size distribution; **c.** metal matrix microstructure generated in Packing2D before and after the cleaning up of acute angles (on the top and bottom respectively); **d.** zoom on the generated matrix microstructure.

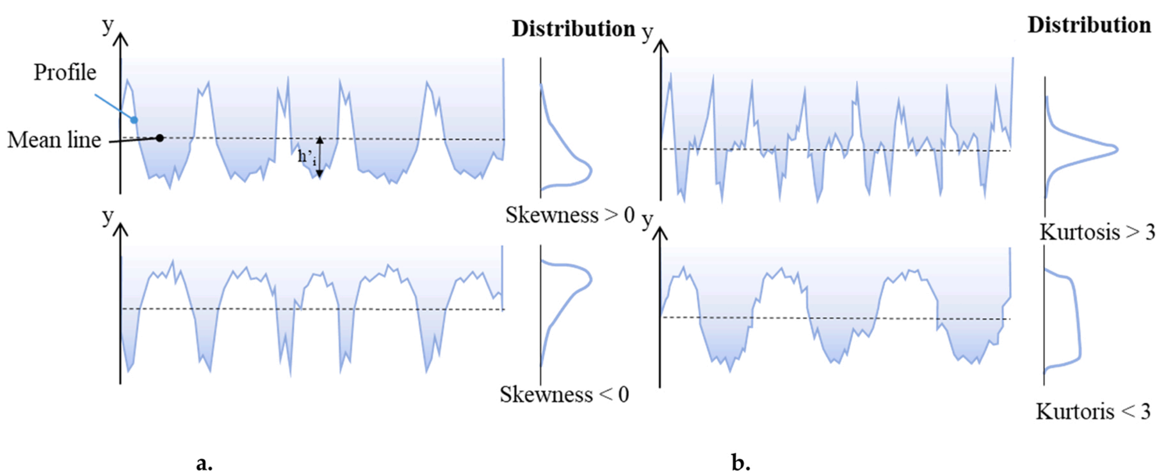

Fig. 7. Illustration of **a.** skewness R_{sk} and **b.** kurtosis R_{ku} together with the respective distribution functions (the blue areas stay for the matrix microstructure) [44], modified.

Table 2
Initial roughness parameters of the degradable microstructure.

R_a (μm)	R_q (μm)	R_{sk} (-)	R_{ku} (-)
0.5331	0.6048	0.5804	2.0864

the tangential direction δ_t (Mode II) are calculated from the relative displacement of its field nodes once the interface between grains begins to open (Mode I) or slide (Mode II) (Fig. 9a.), using the contact detection algorithm explained in [35]. In this way, the intergranular contact stress can be described by the CZM constitutive law that is illustrated in Fig. 9b. (the subscripts n and t are omitted because the constitutive law is assumed to be the same in the normal and tangential directions). Different functional forms of the cohesive law are proposed in the literature (e.g., triangular, exponential, or trapezoidal), but for the sake of simplicity, a simple triangular law is used in this work. It is characterized by an initial elastic regime defined by the initial contact stiffness k_0 that defines a linear increase of the contact pressure p with the detection distance δup to the reaching of the limit value $p_{\lim}$. Once this threshold is reached, the stress p decreases while the intergranular detection distance δ continues to increase until a residual value δ_{res} is achieved. Ignoring for a moment the fatigue, the Fig. 9b. then describes

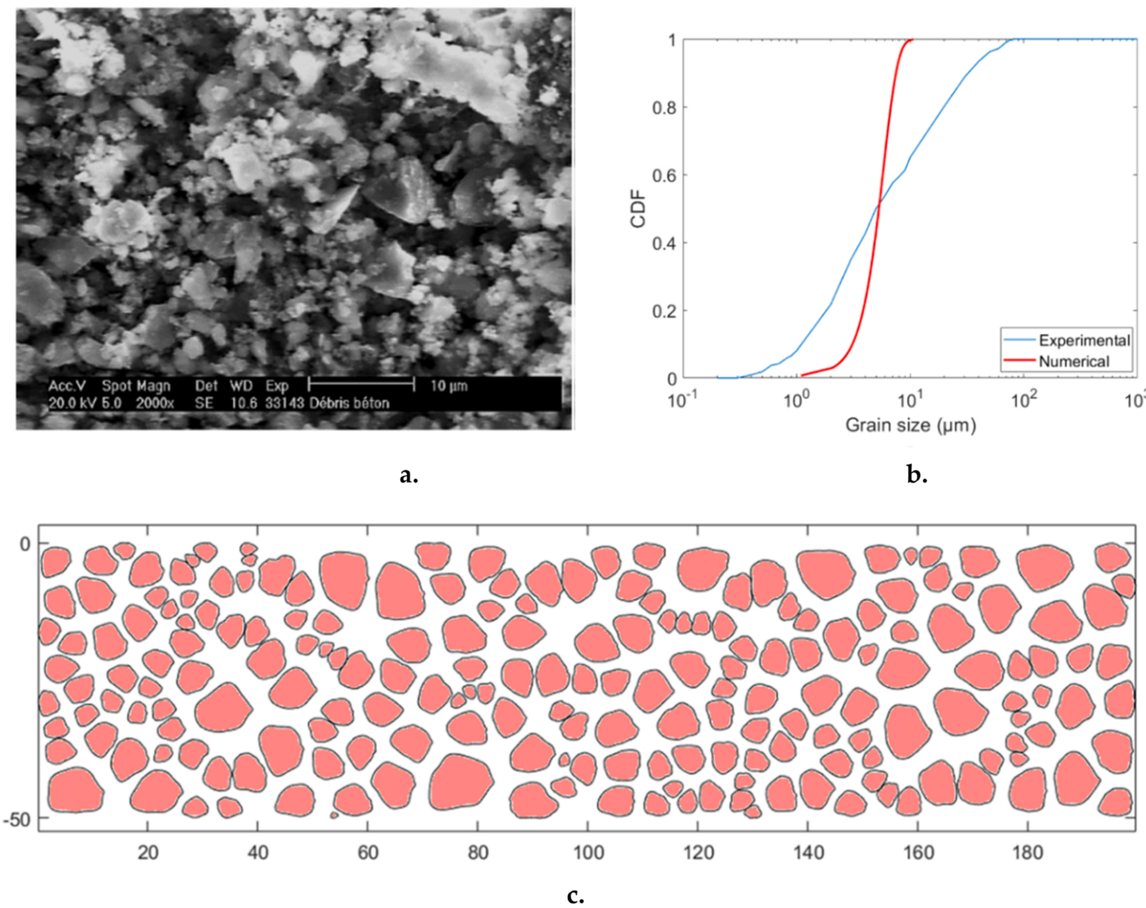

Fig. 8. Definition of rock debris: **a.** observed by SEM [24] **b.** comparison between the experimental and numerical grain size distribution; **c.** rock debris generated in Packing2D.

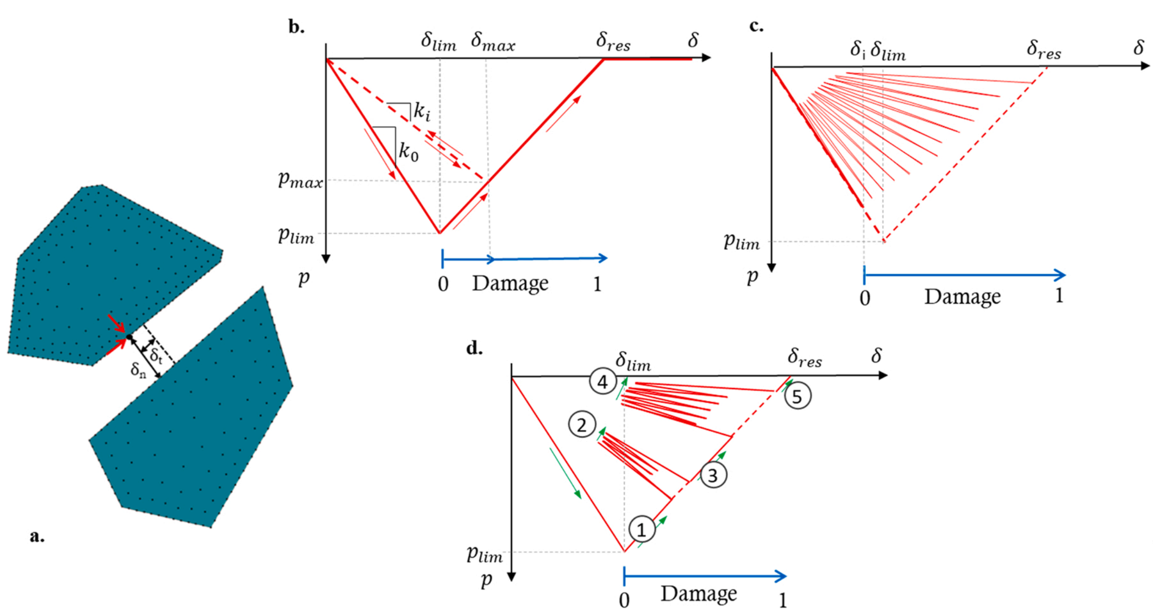

Fig. 9. a. Cohesive contact between two grains (δ_n :normal gap;δ_t :tangential gap) **b.** Monotonous CZM law; **c.** Fatigue CZM with degradation starting in the elastic domain ($p_{\lim}$ is never reached); **d.** CZM accounts for monotonous(①,③ and ⑤) and fatigue degradation (② and ④).

completely this monotonic degradation: in the elastic range the intergranular detection distance is still too small ($\delta < \delta_{\lim}$), but once the threshold is reached ($\delta > \delta_{\lim}$) the intergranular fracture becomes increasingly important ($\delta = \delta_{\max}$, i.e., the maximum gap even reached) leading to grain detachment. Typically, this phenomenon is described in terms of contact resistance and contact stiffness degradation ($k_i < k_0$

and $p_{\max} < p_{\lim}$, respectively in Fig. 9b.) controlled in turn by the damage parameter D, i.e. an internal variable ranging from 0 (intact bond) to 1 (broken bond). The CZM is then initialized at the beginning of the simulation; the damage parameter D is stored at each node of each grain border and updated at each time step. Then, for a monotonous degradation, the damage parameter starts to increase when $\delta = \delta_{\max} > \delta_{\lim}$ as:

$$D_i = \frac{\delta_{\max} - \delta_{\lim}}{\delta_{res} - \delta_{\lim}} \tag{1}$$

Damage may also occur by fatigue if the degradation (i.e., stiffness and strength reduction at grains boundary) is related to contact stress cycles occurring even in the elastic part of the triangular law, as illustrated in Fig. 9c. Fatigue degradation is necessary to describe wear as a slow phenomenon caused by the continuous passage of rock debris. This progressive failure is controlled by the fatigue damage parameter dD_fdefining the rate of damage increase with the increment of the contact stress at a given contact node:

$$dD_f = \frac{D_i - D_{i-1}}{p_i - p_{i-1}} = \frac{dD}{dp} \tag{2}$$

where i is a given time step of the simulation. dD_f is imposed as a constant parameter during the simulation. It means that the smaller is the fatigue damage parameter dD_f, the smaller is the increment of the damage after a certain number of stress cycles. In this way, fatigue damage is defined as a function of the current contact stress and the fatigue damage parameter:

$$D_i = D_{i-1} + \frac{p_i - p_f}{p_{\max} - p_f} \bullet dD_f \bullet (p_i - p_{i-1}) \tag{3}$$

It means that the damage increment $D_i - D_{i-1}$is proportional to the contact stress increment $(p_i - p_{i-1})$ multiplied by the fatigue damage rate dD_f. The increment of damage is more significant if the load is high than if it is low.

In both cases (monotonous and fatigue damage), if the bond is already broken (i.e. $D_i = 1$), the cohesion is set to the residual value, assumed equal to zero in this study. Finally, coupling cohesive law with fatigue, failure may happen both in monotonous and fatigue-related ways. The complexity of this law does not allow the two responses (monotonic and cyclic) to be decoupled, since they could then occur without one prevailing over the other if degradation takes place in the plastic field, as schematized in Fig. 9d. where monotonous damage ①,③, and ⑤ alternates with the fatigue ② and ④.

The choice of CZM parameters is not straightforward. Several attempts have been made to calibrate them [52–54]; however, there is no standard procedure. A sensitivity analysis will be performed in next Section 3.

2.4. Scaling of the computational time

Defining the grains of the metal matrix as deformable allows for greater accuracy in the results compared to considering them rigid as well as the definition of continuous strain and stress fields. Yet, this aspect, together with the definition of the CZM + fatigue contact law, yields a very complex model with a relatively large computation time ranging from about a dozen days to a few months depending on the contact parameters chosen. For instance, considering the minimal nodal distance $d_{nodes} = 0.1\mu m$, the Young modulus of the metal surface $E_m = 210 GPa$ and the volumetric mass $\rho_m = 8600 kg/m^3$, the critical time step is:

$$\Delta t = \frac{d_{nodes}}{\sqrt{\frac{E_m}{\rho_m}}} \approx 10^{-11} s \tag{4}$$

While the ratio $\sqrt{E_m/\rho_m}$ is maximum compression wave celerity v_w. It is possible to speed up the simulation by playing on certain parameters, being careful not to alter the physics of the problem. For instance, reducing Young's modulus by a factor of 100 increases the critical time step Δt by a factor of 10, i.e. the simulation is accelerated by a factor of 10. Furthermore, as mentioned in Section 2.1, the cutting speedv_t is also taken in an order of magnitude larger than that generally used to cut stone by drilling. This choice is reasonable as long as certain scalar parameters are preserved: the ratio between the cutting speed and the wave propagation v_t/v_w should remain small enough to avoid unphysical dynamic couplings, while the inertia number I in the granular debris should be controlled so as not to change the granular flow regime. This last parameter is defined as:

$$I = \frac{\dot{\gamma} d_d}{\sqrt{\frac{p}{\rho_d}}} \tag{5}$$

Where $\dot{\gamma}$ is the shear rate of debris flow, d_d is the average debris grain size and ρ_d is the volumetric mass of debris grains. The main real and numerical quantities are defined in Table 3. As we can observe, the ratio v_t/v_w is still smaller than the unit, while the inertia number I is still in the range of the dense flow regime [42].

3. Results

The complexity of such a model is in the definition of the CZM parameters as well as the lack of experimental observations at the local scale. Therefore, by using the qualitative information of Section 2 and the macroscopic predictive model [29], the aim is to describe the abrasive wear phenomenon by quantifying the detachment and ejection of matrix grains.

3.1. Damage and wear analysis

The wear analysis is performed following the damage process of each metal grain and assuming that they are quickly removed from the system to fulfil what is discussed in the Introduction, namely that wear is mainly caused by rock debris, while the worn metal grains are immediately evacuated from the system with recirculating water. This experimental evidence is reproduced in the numerical simulation by imposing a deactivation condition on the displacement l_{de} for detached grains. Grains are "ejected" (i.e. instantly removed from the simulation) when they reach a displacement equal to their equivalent half-size $d_m/2$, disappearing from the simulation environment:

$$l_{de} = \frac{d_m}{2} \tag{6}$$

Considering the average grain size $d_m = 2.3\mu m$ (Table 1), then $l_{de} = 1.15\mu m$.

Along these lines, the position of the damage front in the matrix ("damage level h_d") is measured in terms of the average matrix depth and ignoring grains that reached the maximum damage level $D = 1$ monotonously (Eq. (1)) or by fatigue (Eq. (3)). This average level is labelled as $h_d(t)$ and is illustrated in Fig. 10. Similarly, the current matrix surface ("wear level h_w″) is measured in Fig. 10 as the average matrix depth including damaged grains that are still in the system. In other words, the wear level is the average level of the contacting surface.Both the damage and wear levels are measured from the onset of the contact ($h_m = 0\mu m$). It is straightforward that, at the early stage of the contact

Table 3
Real and numerical parameters for the definition of the scaling quantities.

	p_n [MPa]	v_t [m/s]	E_m [MPa]	ρ_m [kg/m^3]	ρ_d [kg/m^3]	v_t/v_w [-]	I [-]
Real	3.4	5	211,000	8900	2700	$\approx 10^{-3}$	0.056
Num.	3.4	50	2110	8900	27	$\approx 10^{-1}$	0.025

($t = t_1$), no grain has broken its bonds yet, therefore $h_d(t_1) = h_w(t_1)$, as illustrated in Fig. 10a.

How the degree of damage and wear varies over time depends on the shape of the cohesive contact law and its rate of degradation. Following this procedure, Fig. 11 shows the time evolution of damage and wear for a particular case study, the parameters of which are listed in Table 4 for the CZM contact law. Concerning the Mohr-Coulomb law, the friction coefficient is $\mu = 0.3$ as mentioned in Section 4.2, while the initial stiffness $k_0 = 10^6 MPa/\mu m$, i.e., the same value is used for the Mohr-Coulomb and the CZM contact law.

Notice that the stiffness parameter k_0 (in both the Mohr-Coulomb and the CZM contact laws) has to be large enough to avoid artificial overlapping between grains, in order for the elastic deformation to be mostly accommodated by the deformation of the grains themselves. We must however keep in mind that if contact laws are too stiff, it will increase the computation time of the simulation. For these reasons, in the following, the value $k_0 = 10^6 MPa/\mu m$ is chosen as a reasonable compromise.

The first stage ① in Fig. 11 consists of the initialization of damage (run-in in Fig. 11b.) that accumulates in the contact zone. During this phase, the wear rate is negligible. Then, in stage ② grains are continuously detached and ejected from the system (steady-state of wear rate in Fig. 11b.). Here the damage and wear levels vary in a quasi-linear way, defining constant damage and wear rate. Finally, in ③, damage propagates toward the inner matrix microstructure, coming closer to the non-degradable part and reaching a plateau. Since the non-degradable part does not exist in reality, this last phase has no physical meaning. The damage and wear curves are approximately parallel, meaning that the grains are damaged and then ejected at almost the same rate.

Locally, the stress concentrates on the surface in contact with the rock grain asperity, thus validating the macroscopic study [29], namely that the abrasive power depends on the asperity of the debris particles. The localization of stress is illustrated in Fig. 12 in terms of Von Mises and tangential Cauchy stress.

3.2. On the effect of the ultimate strength

The results shown in the previous section correspond to a defined selection of the CZM parameters. However, the definition of the shape and degradation of the CZM law is not straightforward. In this Section, a first study is performed to evaluate the influence of the ultimate strength p_{lim} on the damage and wear response. The Mohr-Coulomb parameters are the same as defined in Section 3.2, while the CZM parameters are listed in Table 5. The ultimate strength p_{lim} is successively set to 50, 100, 200, 400 and 800 MPa as shown in Fig. 13a.: the lower the threshold p_{lim}, the smaller the elastic range of the law, enhancing the plastic breakdown. The ultimate strength, therefore, changes the form of the triangular contact law and is a measure of the material resistance of the metal, since the higher the material resistance, the higher the ultimate strength p_{lim} is expected to be. Complementary further studies could therefore be useful in quantifying this relationship.

The temporal evolution of damage and wear levels are plotted in Fig. 13b. for the different values of p_{lim} following the procedure described in Section 3.2. Whatever the value of p_{lim}, there is always an offset between the damage and wear level. This delay in the wear response is more evident for $p_{lim} \geq 400 MPa$. Moreover, the steady state of damage and wear rate are always preceded by a run-in and followed by a plateau at contact with the non-degradable matrix. Nevertheless, by increasing the ultimate strength p_{lim}, not only is there a reduction in the rate of damage and wear (reduction of the slope of the curve corresponding to the steady-state) but also a change in the profile that becomes less and less linear. This occurrence can be explained by observing the propagation of damage, which in turn may be related to the surface topography of the degradable matrix.

For low values of ultimate strength p_{lim}, the degradation is very quick with a well-defined vertical gradient from the surface (where $D = 1$ for almost all the grains) towards the inner sub-surface, as illustrated in Fig. 14a. for $p_{lim} = 100 MPa$ and for the different wear levels corresponding to the values $P'_{w,i}$ given in Fig. 13b. On the other hand, for high values of p_{lim} (800 MPa in Fig. 14b.) the damage does not follow a well-defined path but clusters of damaged grains are evident throughout the degradable part as illustrated in Fig. 14b. for the values $P''_{w,i}$ in Fig. 13b.

This phenomenon leads to a characteristic topography of the contact surface and can be explained by looking at the temporal evolution of the roughness of the matrix surface. The arithmetic and mean deviation of the roughness profile follow the rate of damage and wear whatever the value of p_{lim} is (Fig. 15a.-b.): the onset of damage defines a favourable condition for the grains detachment and wear, thereby increasing the roughness of the profile. These results are consistent with what can be found in the literature on the subject [55–57]. In the end, it is rather obvious that, when the degradable surface is almost completely worn, the roughness is greatly reduced. This is purely related to the presence of the non-degradable surface which is perfectly flat.

Some fluctuations of the roughness profile are observed in Fig. 15a.,

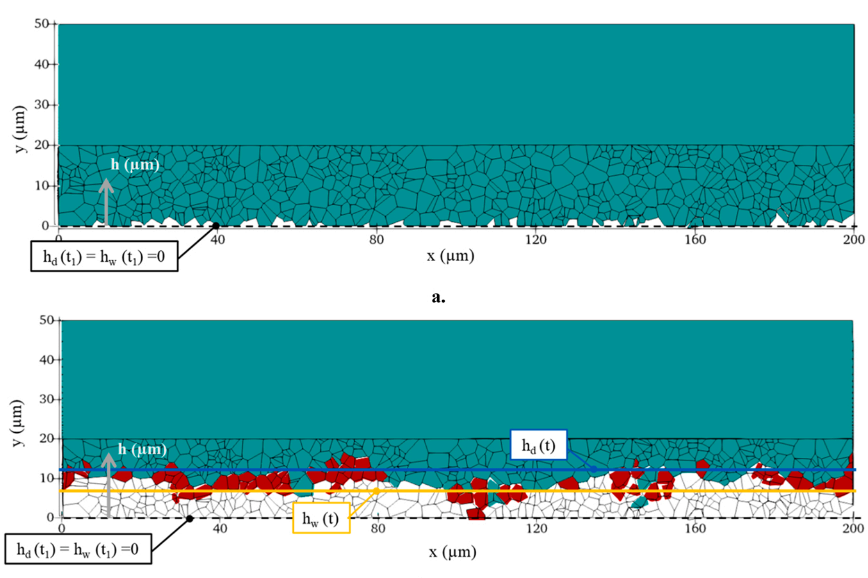

Fig. 10. Schematization of the measure of the damage and wear level (h_d and h_w) computed from the contacting surface at **a.** $t = t_1$ initial stage of the contact; **b.** $t = t_i$: after a certain number of passages of the debris flow. Grains start to lose cohesion reaching the maximum damage possible (grains in red, $D = 1$) and detaching from the microstructure. This phenomenon leads to a variation of the average contact surface and, therefore the wear level h_w (in yellow, $l \geq l_{de} = 1.15\mu m$) and damage level h_d (in blue, $D = 1$), with respect to the initial profile. Grains in white have been already ejected while the initial profile is plotted in a black dot line.

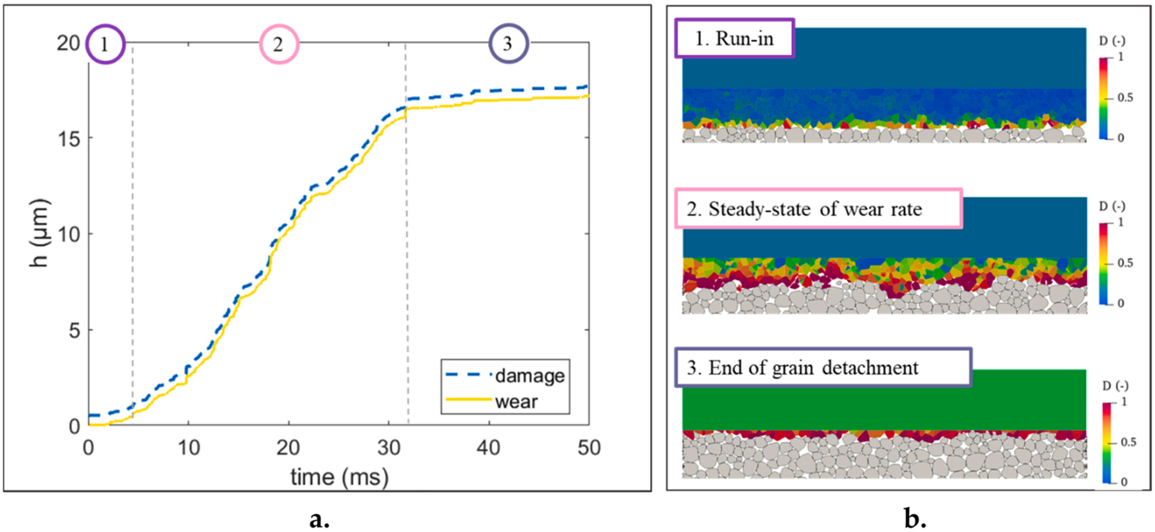

Fig. 11. **a.** Temporal evolution of the damage and wear level with the sub-division in three characteristic phases: ① Run-in; ② Steady-state of wear (and damage) rate; ③ End of grain detachment; **b.** snapshots of the three phases.

Table 4
CZM fatigue parameters.

k_0 (MPa/µm)	$p_{\lim}$ (MPa)	δ_{res} (µm)	p_{res} (MPa)	dD_f (MPa^{-1})
10^6	800	0.002	0	0.05

they can be related to the smoothing of the surface caused by the debris passage (damage grains are equally distributed along the contact surface and can be easily removed and ejected as illustrated in Fig. 14a.). On the other hand, the increase and subsequent reduction in roughness on the profile in Fig. 15b. ($p_{\lim} = 800MPa$) deserves a few more observations: the average and quadratic roughnesses follow the evolution of the wear (and damage) with time. This phenomenon is important to further investigate the damage propagation observed in Fig. 14b. The presence of "clusters" of damaged grains leads to a propagation of damage towards the interior of the microstructure and is thus hindered by the presence of the non-degradable matrix. This phenomenon thus explains the characteristic bilinear steady-state of wear rate, which could then be divided into a stationary state and a perturbed steady-state (i.e., perturbed by the non-degradable matrix).

Moreover, to better understand the effect of the spatial distribution of damage on the topography of the degradable surface, it is necessary to analyze the temporal evolution of the moments of third and fourth-order. As introduced for the moments of first and second order, the skewness and the kurtosis evolutions are characterized by fluctuations when $p_{\lim} = 100MPa$. The variation of skewness between positive and negative values indicates the absence and subsequent generation of sharp valleys on the profile where pressure can concentrate (see Fig. 12), thereby increasing the damage level and leading to the grain detachment, which in turn is responsible for the flattening of the surface (the increase of skewness). For the same reasons, the kurtosis firstly increases and then decreases to values lower than 3, defining the flattening of the profile roughness. For $p_{\lim} = 800MPa$, the skewness is initially positive during the wear run-in and the beginning of the steady-state of wear rate, then it reduces to values slightly lower than zero, meaning that the profile is approximately symmetrical in terms of the height of peaks and valleys but with a slight majority of valleys. The persistence of negative values of skewness may be related to the slow wear process defined by the high ultimate strength which causes the valleys to be smoothed slowly and after several passages of the debris flow. The kurtosis starts to values lower than 3, indicating that the surface remains almost flat during the run-in and the initial steady state of wear, and then, when damage reaches the non-degradable part (perturbed steady-state), the kurtosis increases slightly remaining still close to or lower than 3.

The differences in the behavior described above may also be related to the way the matrix degrades, i.e. whether de-cohesion is predomi-

Table 5
CZM fatigue parameters.

k_0 (MPa/µm)	$p_{\lim}$ (MPa)	δ_{res} (µm)	p_{res} (MPa)	dD_f (MPa^{-1})
10^6	[50, 100, 200, 400, 800]	0.002	0	0.001

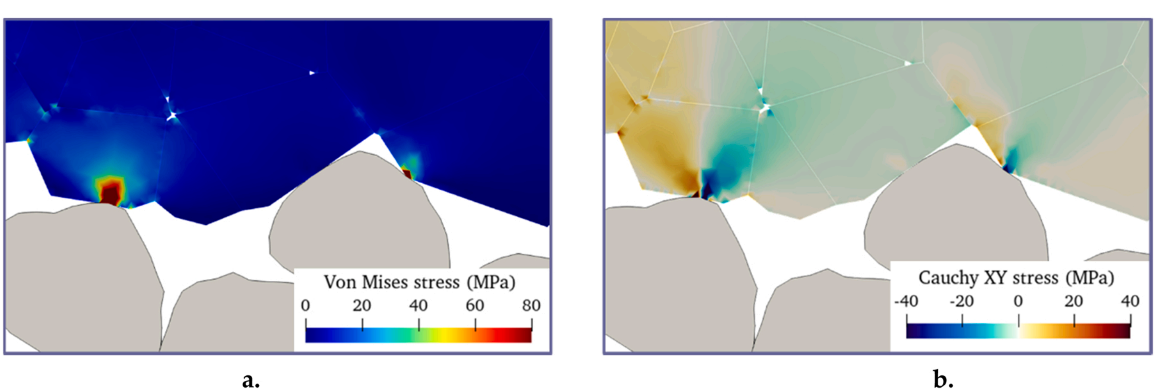

Fig. 12. Localization of the contact stress at the matrix-debris interface in terms of **a.** Von Mises **b.** Cauchy shear stress.

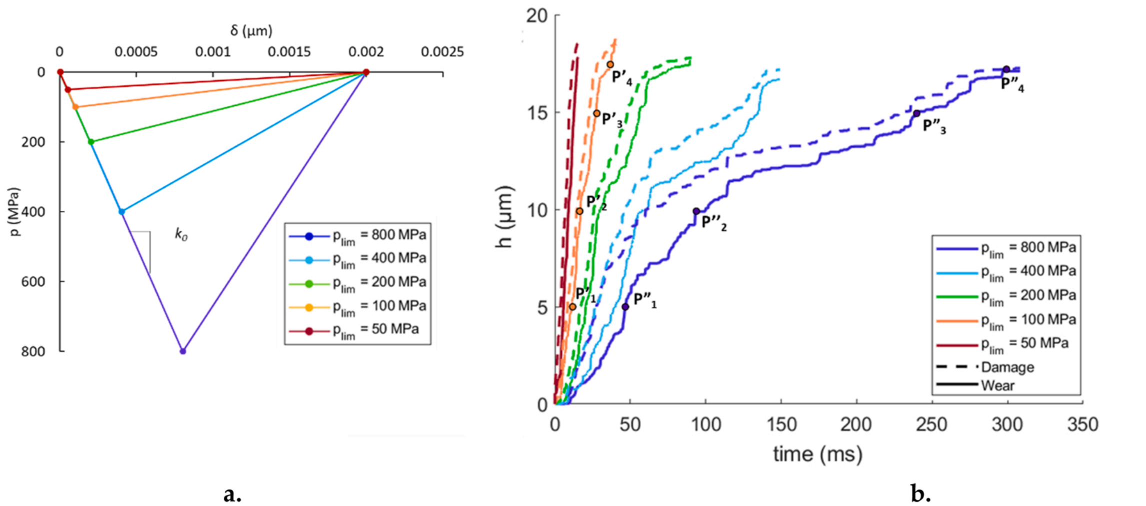

Fig. 13. a. Effect of the ultimate strength p_{lim}on the bilinear CZM laws b. Temporal evolution of damage (dotted lines) and wear (continuous lines) for different values of p_{lim}.

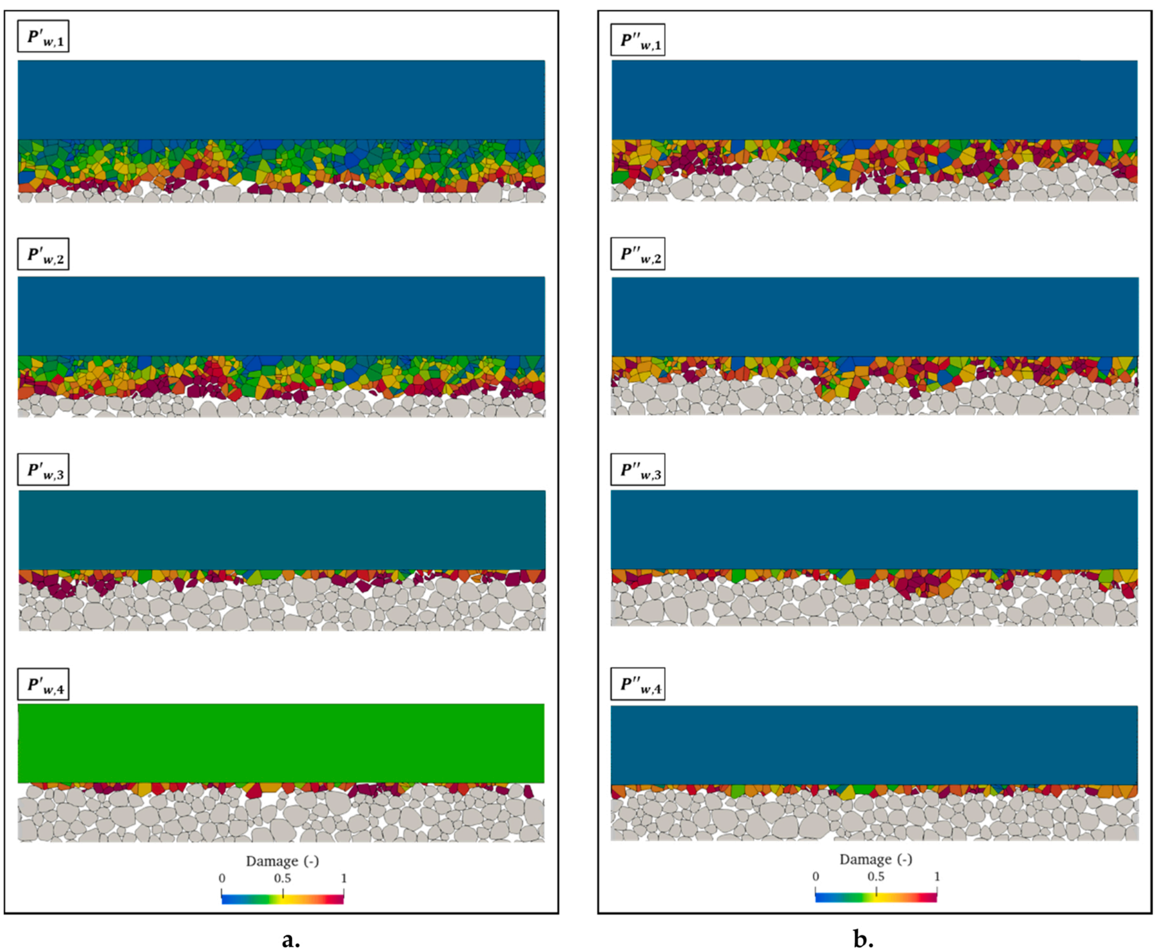

Fig. 14. Snapshots of the matrix degradation **a.** $p_{\lim} = 100MPa$; **b.** $p_{\lim} = 800MPa$ (in both cases $dD_f = 10^{-3}MPa^{-1}$).

nantly monotonic or fatigue (Fig. 9). Although it is not possible to rigorously quantify the shares of the static process from the cyclic one in the implemented CZM law, fatigue degradation seems to be mainly involved at high ultimate stresses, when the grains are not detached immediately but after several passes of debris particles. For small values of $p_{\lim}$, the wear is very fast: grains are damaged and detached quickly from the matrix but remain in the system for a while before being ejected, thus defining wear no more caused by the debris flow but by the matrix grains themselves. Therefore, the wear associated with the small value of ultimate strength is likely not representative of reality.

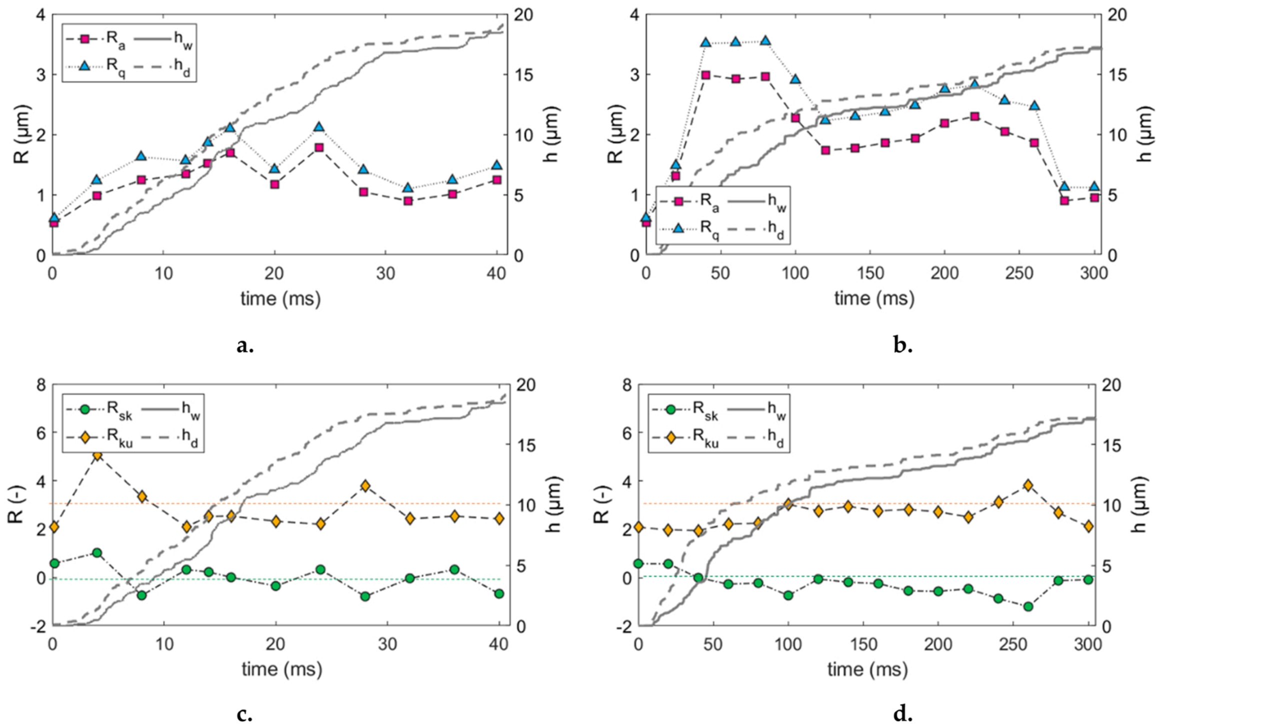

Fig. 15. Definition of the roughness parameters; On the top: Arithmetic $R_a$and standard deviation R_q for: **a.** $p_{\lim} = 100MPa$; **b.** $p_{\lim} = 800MPa$. On the bottom: Skweness R_{sk} and Kurtosis R_{ku} for: **c.** $p_{\lim} = 100MPa$; **d.** $p_{\lim} = 800MPa$.

3.3. On the effect of the fatigue damage parameter

The rapidity of damage and wear processes can be numerically controlled by the fatigue damage parameter dD_f. Physically, this parameter is an indicator of the fact that the metal matrix does not degrade immediately on direct contact with the debris, but there is a relative motion between the tool and the debris flow that causes degradation to occur by successive passages of the debris itself.

In this analysis, the parameters in Table 4 and Table 5 are used for the Mohr-Coulomb and the CZM fatigue laws, respectively; except for the dD_f that is successively set to 0.1,0.5, 0.01, 0.001 and 0.0001 MPa^{-1}: the higher the fatigue parameter, the fewer stress cycles are required for fatigue-related degradation, thus favouring damage and grain detachment (Fig. 9c-d). The temporal evolutions of damage and wear for different values of $dD_f$are plotted in Fig. 16. Notice that the curves for $dD_f = 10^{-3}MPa^{-1}$ are the same as in Fig. 13b for $p_{\lim} = 800MPa$.

The curves in Fig. 16 follow the same behavior observed in Fig. 13b: the reduction on dD_f is comparable to the increase of $p_{\lim}$. In other words, as dD_f increases, the variations of h_d and h_w with time become less and less linear with a real transition of behavior for $dD_f = 10^{-3}MPa^{-1}$. As already explained in Section 3.2, these differences can be related to the damage propagation within the matrix microstructure (Fig. 17) and the roughness of the contact surface (Fig. 18). More specifically, the propagation of damage for $dD_f = 0.1MPa^{-1}$ is quite linear from the contacting surface to the continuum matrix, it is comparable to what is observed in Fig. 14a. for $dD_f = 10^{-3}MPa^{-1}$ and $p_{\lim} = 100MPa$.

The temporal evolution of the roughness profile for $dD_f = 0.1MPa^{-1}$ is plotted in Fig. 18 in terms of average and standard deviation roughness (Fig. 18a.) and skewness and kurtosis (Fig. 18b.) and together with the damage and wear time variations. It is worth noting that the behavior is broadly comparable to that observed in Fig. 15a. and therefore the same observations made in Section 3.2 apply.

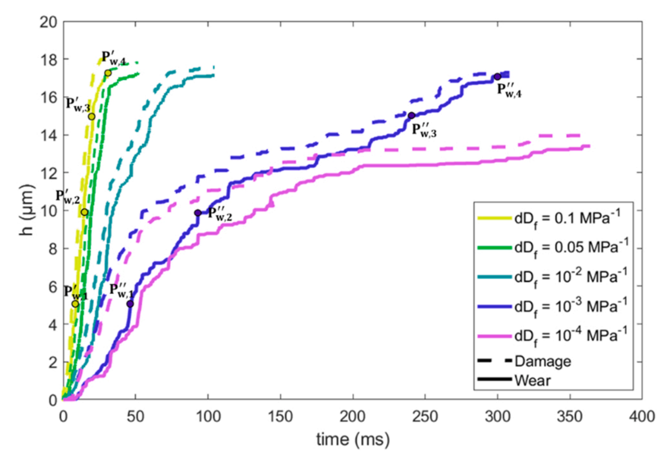

Fig. 16. Temporal evolution of damage (dotted lines) and wear (continuous lines) for different values of dD_f.

4. Discussion

Although ultimate strength and fatigue parameters are two distinct physical parameters, they lead to a very similar degradation process: reducing the ultimate strength or increasing the fatigue parameter results in a faster wear process, which is also evident in terms of damage propagation and contact surface roughness. In particular, large fatigue damage parameter *dDf* may lead to the formation of the third body of metal particles that can abrade the metallic surface. This would define a wear process different from the one observed since the experimental wear is actually caused by debris grains and not by the metallic grains themselves.

By increasing the ultimate strength and decreasing the fatigue parameter, the degradation of the surface becomes slower and slower with the generation of damaged grains clusters leading to a characteristic surface roughness. This phenomenon could occur because fatigue

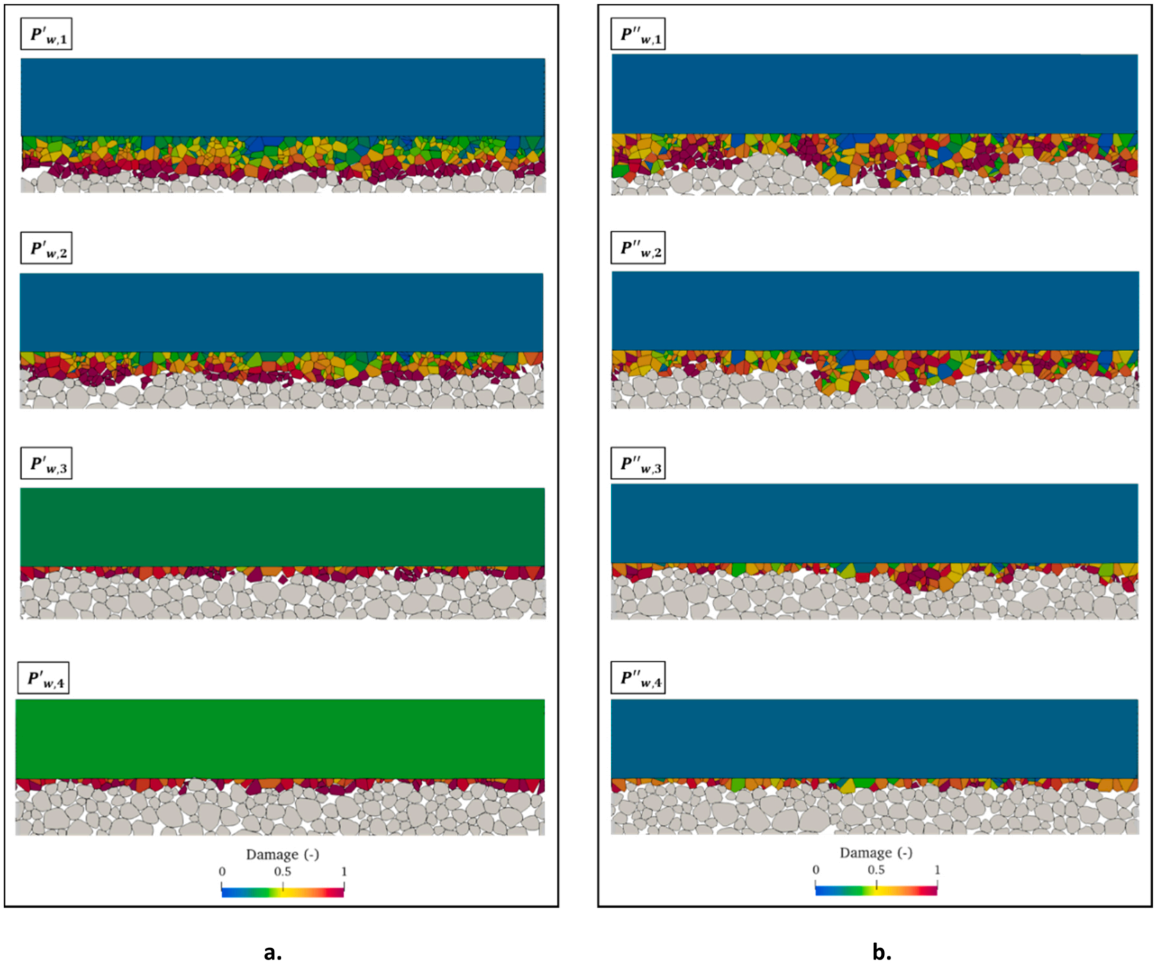

Fig. 17. Snapshots of the matrix degradation **a.** $dD_f = 0.1 MPa^{-1}$; **b.** $dD_f = 0.001 MPa^{-1}$ (in both cases $p_{\lim} = 800 MPa$).

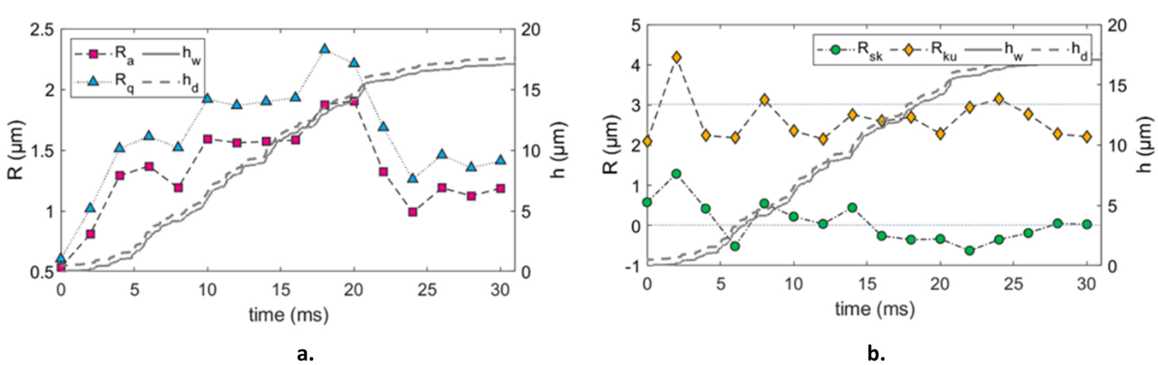

Fig. 18. Definition of the roughness parameters for $dD_f = 0.1 MPa^{-1}$: **a.** average (R_a) and standard deviation (R_q)for: **b.** Skweness (R_{sk}) and Kurtosis R_{ku}.

damage prevails over monotonic damage.

Fig. 19 shows the wear rate as a function of the ultimate strength and fatigue damage parameter. As already mentioned, by increasing the ultimate strength or decreasing the fatigue parameter, the steady-state becomes more and more disrupted by the presence of the non-degradable matrix, thus explaining the relative considerable difference in the assessment of the average wear rate dh_w.

Power law fits provided in Fig. 19 seem acceptable. In particular, the wear rate is inversely proportional to the ultimate strength $p_{\lim}$ (exponent $\chi_2 \cong -1$in Fig. 19a.) and is also almost proportional to the square root of the fatigue damage parameter dD_f (exponent $\chi_4 \cong 0.5$in Fig. 19b.) except for small values of dD_f where a power law is not able to fit the numerical results. Nevertheless, as will be explained later, low dD_f values seem to be more representative of the physical phenomenon than the larger ones.

The wear rate obtained in this study is several orders of magnitude higher than that obtained experimentally in the proximity of the diamond (~0.1 μm/s, [24,29]). This discrepancy is explained by the numerical need to accelerate time in the simulations (see Section 3.1), which therefore do not reflect the real-time scale. It is worth reminding that the aim here is not to predict wear numerically but to better understand the phenomenon. In particular, it has been seen how the shape and degradation of the CZM law (i.e. the choice of parameters) influence the evolution of surface roughness, the damage gradient, and thus the

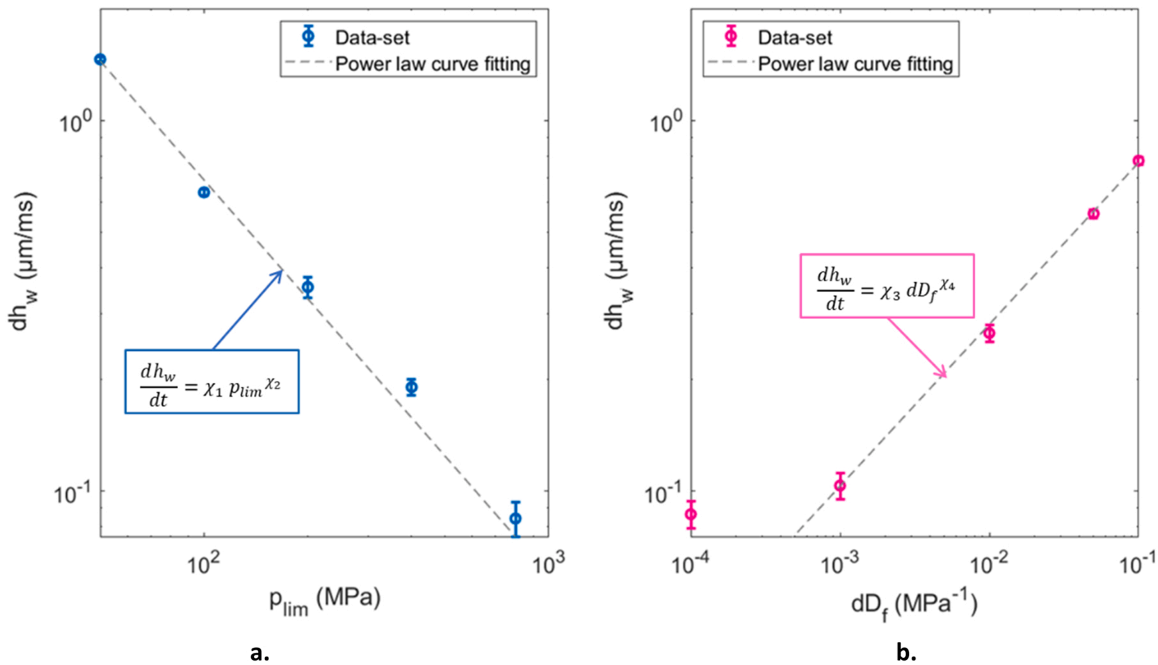

Fig. 19. Wear rate as a function of **a.** the ultimate strength $p_{\lim}$ when $dD_f = 0.001MPa^{-1}$ ($\chi_1 = 93.57$; $\chi_2 = -1.066$) **b.** the fatigue parameter $dD_f = 0.001MPa^{-1}$ when $p_{\lim} = 800MPa$ ($\chi_3 = 2.099$;$\chi_4 = 0.4363$; $R^2 = 0.9099$).

wear itself. High fatigue parameter values (or low ultimate strength values) overestimate the wear process because the damage is so rapid that the detached grains remain in the system before they are ejected, becoming abrasives for the matrix itself (Fig. 20).

This phenomenon is clearly far from what is observed experimentally. Therefore, a good representation should consider a small fatigue parameter (not larger than 0.001 MPa^{-1}) and a realistically large value of ultimate strength (not smaller than 400 MPa).

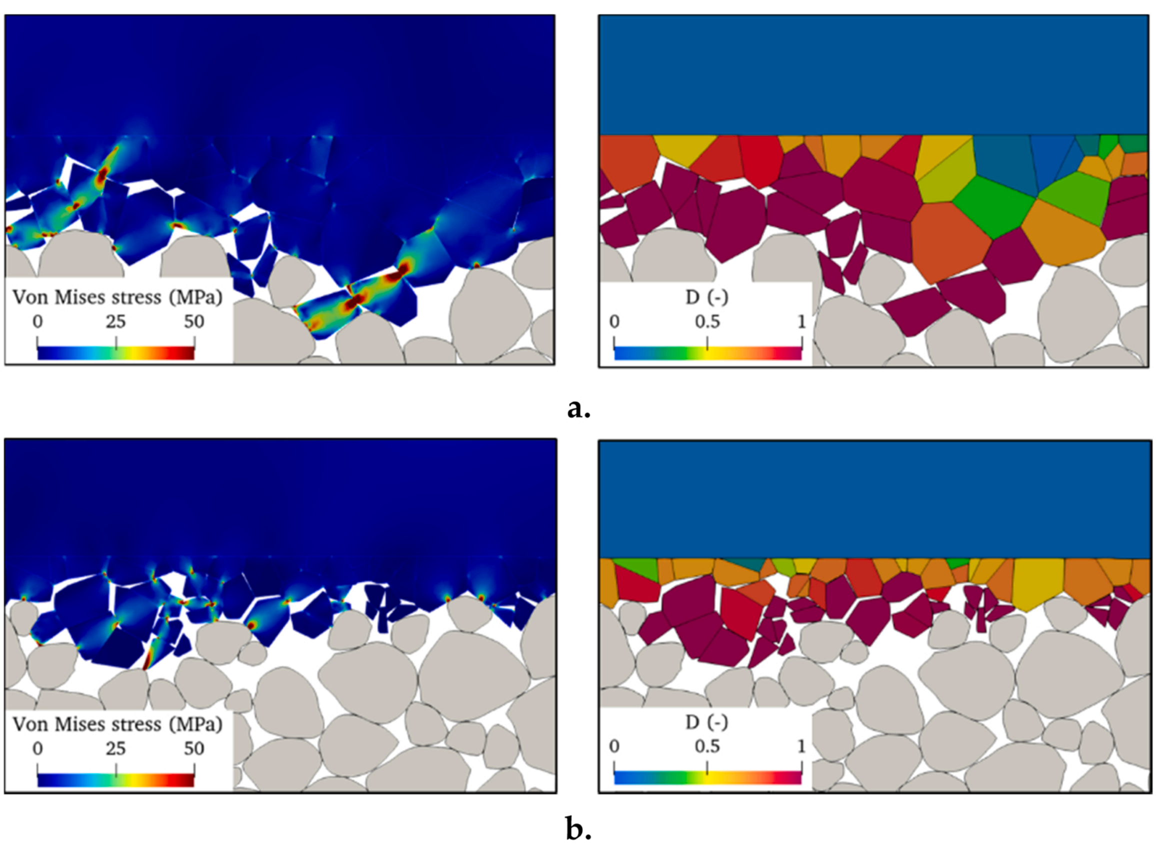

Fig. 20. Snapshots of matrix wear in terms of Von Mises stress (right) and damage parameter D (left) if **a.** $p_{\lim} = 100MPa$ and $dD_f = 0.001MPa^{-1}$; **b.** $p_{\lim} = 800MPa$ and $dD_f = 0.1MPa^{-1}$.

5. Conclusions

The proposed model offers a suitable tool for understanding abrasive wear phenomena that cannot be observed experimentally or at a macro scale.

The strength and the originality of the model here proposed lies in its ability to control aspects such as grain shape and size, as well as the implementation of a complex constitutive law, namely the CZM with fatigue. In this sense, the proposed model succeeds in complementing what has already been analysed experimentally and numerically using a large-scale model by offering useful suggestions for its interpretation. In particular, the qualitative observations of the stress field in the metal matrix validate one of the assumptions on which the macroscopic predictive model is based, namely that wear is caused by the asperities of the rock debris.

Moreover, the temporal evolution of the contact surface follows that of damage and wear and thus offers an alternative reading key to abrasion. Furthermore, the roughness profiles obtained are consistent with what is already found in the literature, thus bringing additional validation to the model.

The calibration of the CZM + fatigue parameters leads to the conclusion that an optimal solution is to avoid large fatigue damage parameters and ensure that the strength parameters are large enough to account for the fatigue effects also in the elastic domain, ensuring they are caused by the debris flow. For this purpose, it will be useful to consider a thicker degradable region of the matrix since the damage propagation is limited by the non-degradable part (introduced to reduce the cost of the simulation).

To better quantify this case study, however, it is necessary to complement it with other numerical tests. In particular, uniaxial compression tests could clarify the relationship between ultimate strength and material strength.

Furthermore, considering that wear is caused by the asperities of rock debris, these can be regarded as indenters capable of abrading the metal surface after repeated passes. Thus, the ultimate strength could be assessed by numerically simulating the behavior of the same metal matrix subjected to a multiple scratch test. This type of test has in fact already been used to derive the constitutive law of the macroscopic model built by the same authors, and indeed led to a satisfactory prediction of the experimental wear rate.

Statement of Originality

As corresponding author, I Adriana Quacquarelli, hereby confirm on behalf of all authors that: This manuscript is original, has not been published before and is not currently being considered for publication elsewhere. The manuscript has been read and approved by all named authors and that there are no other persons who satisfied the criteria for authorship but are not listed. The paper does not contain material which has been published previously, by the current authors or by others, of which the source is not explicitly cited in the paper.

Declaration of Competing Interest

The authors declare that they have no known competing financial interests or personal relationships that could have appeared to influence the work reported in this paper.

Data Availability

Data will be made available on request.

Acknowledgment

This work is supported by Umicore Specialty Powders France, for which the authors are grateful.

Appendix A. Supporting information

Supplementary data associated with this article can be found in the online version at doi:10.1016/j.triboint.2022.108126.

References

[1] Petrica M, Badisch E, Peinsitt T. Abrasive wear mechanisms and their relation to rock properties. Wear 2013;308(1–2):86–94. https://doi.org/10.1016/j.wear.2013.10.005.
[2] Woldman M, Van Der Heide E, Tinga T, Masen MA. The influence of abrasive body dimensions on single asperity wear. Wear 2013;301(1–2):76–81. https://doi.org/10.1016/j.wear.2012.12.009.
[3] Masen MA, De Rooij MB, Schipper DJ. Micro-contact based modelling of abrasive wear. Wear 2005;258(1–4):339–48. https://doi.org/10.1016/j.wear.2004.09.009.
[4] Kato K, Adachi K. Wear mechanisms. Modern Tribology Handbook: Volume One: Principles of Tribology. CRC Press; 2000. p. 273–300.
[5] Berthier Y. Maurice Godet's third body. In: Dowson D, Taylor CM, Childs THC, Dalmaz G, Berthier Y, Flamand L, Georges J-M, Lubrecht AABT-TS, editors. The Third body concept interpretation of tribological phenomena, 31. Elsevier; 1996. p. 21–30.
[6] Descartes S, Berthier Y. Rheology and flows of solid third bodies: Background and application to an MoS1.6 coating. Wear 2002;252:546–56. https://doi.org/10.1016/S0043-1648(02)00008-X.
[7] Sin H, Saka N, Suh NP. Abrasive wear mechanisms and the grit size effect. Wear 1979;55(1):163–90. https://doi.org/10.1016/0043-1648(79)90188-1.
[8] Gåhlin R, Jacobson S. The particle size effect in abrasion studied by controlled abrasive surfaces. Wear 1999;224(1):118–25. https://doi.org/10.1016/S0043-1648(98)00344-5.
[9] Misra A, Finnie I. On the size effect in abrasive and erosive wear. Wear 1981;65(3):359–73. https://doi.org/10.1016/0043-1648(81)90062-4.
[10] Larsen-Badse J. Influence of grit size on the groove formation during sliding abrasion. Wear 1968;11(3):213–22. https://doi.org/10.1016/0043-1648(68)90559-0.
[11] Stachowiak GW. Particle angularity and its relationship to abrasive and erosive wear. Wear 2000;241(2):214–9. https://doi.org/10.1016/S0043-1648(00)00378-1.
[12] Swanson PA, Vetter AF. The measurement of abrasive particle shape and its effect on wear. ASLE Trans 1985;28(2):225–30. https://doi.org/10.1080/05698198508981615.
[13] Kato K, Hokkirigawa K, Kayaba T, Endo Y. Three dimensional shape effect on abrasive wear. J Tribol 1986;108(3):346–9.
[14] Woldman M, van der Heide E, Schipper DJ, Tinga T, Masen MA. Investigating the influence of sand particle properties on abrasive wear behaviour. Wear 2012;294–295:419–26. https://doi.org/10.1016/j.wear.2012.07.017.
[15] Quacquarelli A. A Multi-scale Modeling Approach for Diamond Tools Wear. INSA de Lyon; 2021.
[16] Konstanty J, Kim T, Kim S-B. Resistance to abrasive wear of materials used as metallic matrices in diamond impregnated tools. Mater. Sci. Forum 2007;534–536:1125–8. https://doi.org/10.4028/www.scientific.net/MSF.534-536.1125.
[17] Konstanty J. Production parameters and materials selection of powder metallurgy diamond tools. Powder Met 2006;49(4):299–306. https://doi.org/10.1179/174329006×113508.
[18] Konstanty J. Chapter 3 - diamond tool design and composition. In: Konstanty J, editor. Powder Metallurgy Diamond Tools. Amsterdam: Elsevier Science; 2005. p. 39–68.
[19] Konstanty J. In: Konstanty JBT-PMDT, editor. Chapter 7 - Wear properties of the matrix. Amsterdam: Elsevier Science; 2005. p. 113–27.
[20] Konstanty J. Factors affecting diamond retention in stone sawblade segments. Key Eng. Mater. 2003;250:13–20. https://doi.org/10.4028/www.scientific.net/KEM.250.13.
[21] Zhao X, Duan L. A review of the diamond retention capacity of metal bond matrices. Metals 2018;8:307. https://doi.org/10.3390/met8050307.
[22] Borowiecka-jamrozek J, Lachowski J. An analysis of the retention of a diamond particle in a metallic matrix after hot pressing. Arch Foundry Eng 2017;17. https://doi.org/10.1515/afe-2017-0003.
[23] Webb SW. Diamond retention in sintered cobalt bonds for stone cutting and drilling. Diam Relat Mater 1999;8(11):2043–52. https://doi.org/10.1016/S0925-9635(99)00167-3.
[24] T. Commeau, A. Nouveau A. Deborde "Usure De Matrices métalliques dans Un flux De debris," 2017 1 11.
[25] A. Deborde and T. Commeau, "Design of high performance binder by understanding the protrusion and clearance dynamics of diamonds during the cutting process+."
[26] Fabbro S, Marra L, Engel J, Kondratiuk J, Kuffa M, Wegener K. Abrasive and adhesive wear behaviour of metallic bonds in a synthetic slurry test for wear prediction in reinforced concrete. Wear 2021;476(September 2020):203690. https://doi.org/10.1016/j.wear.2021.203690.
[27] Fillot N, Iordanoff I, Berthier Y. Modelling third body flows with a discrete element method—a tool for understanding wear with adhesive particles. Tribol Int 2007;40(6):973–81. https://doi.org/10.1016/j.triboint.2006.02.056.
[28] N. Fillot, I. Iordanoff, Y. Berthier, Simul Wear Mass Balance a Dry Contact, 127, 2004.

[29] Quacquarelli A, Mollon G, Commeau T, Fillot N. A dual numerical-experimental approach for modeling wear of diamond impregnated tools. Wear 2021;478–479 (June):203763. https://doi.org/10.1016/j.wear.2021.203763.
[30] Cundall PA, Strack ODL. A discrete numerical model for granular assemblies. Geotechnique 1979;29(1):47–65. https://doi.org/10.1680/geot.1979.29.1.47.
[31] Iordanoff I, Seve B, Berthier Y. Solid third body analysis using a discrete approach: influence of adhesion and particle size on macroscopic properties. J Tribol 2002; 124(3):530–8. https://doi.org/10.1115/1.1456089.
[32] Mollon G. A numerical framework for discrete modelling of friction and wear using Voronoi polyhedrons. Tribol Int 2015;90:343–55. https://doi.org/10.1016/j.triboint.2015.04.011.
[33] Liu GR, Gu YT. A meshfree method: meshfree weak–strong (MWS) form method, for 2-D solids. Comput Mech 2003;33(1):2–14. https://doi.org/10.1007/s00466-003-0477-5.
[34] Mollon G. A multibody meshfree strategy for the simulation of highly deformable granular materials. Int J Numer Methods Eng 2016;108(12):1477–97. https://doi.org/10.1002/nme.5258.
[35] Mollon G. A unified numerical framework for rigid and compliant granular materials. Comput Part Mech 2018;5(4):517–27. https://doi.org/10.1007/s40571-018-0187-6.
[36] Zhang Y, Mollon G, Descartes S. Tribology International Significance of third body rheology in friction at a dry sliding interface observed by a multibody meshfree model: Influence of cohesion between particles 2020;145(October 2019).
[37] Mollon G, Aubry J, Schubnel A. Simulating melting in 2D seismic fault gouge. J Geophys Res Solid Earth 2021;126(6):1–19. https://doi.org/10.1029/2020jb021485.
[38] Casas N, Mollon G, Daouadji A. DEM analyses of cemented granular fault gouges at the onset of seismic sliding: peak strength, development of shear zones and kinematics. Earth Sp Sci Open Arch 2021:42. https://doi.org/10.1002/essoar.10507128.1.
[39] Hall EO. The deformation and ageing of mild steel: {III} Discussion of results. Proc Phys Soc Sect B . 1951;64(9):747–53. https://doi.org/10.1088/0370-1301/64/9/303.
[40] N.J. Petch, "The Cleavage Strength of Polycrystals," 1953.
[41] Dowson D. A generalized Reynolds equation for fluid-film lubrication. Int J Mech Sci 1962;4(2):159–70. https://doi.org/10.1016/S0020-7403(62)80038-1.
[42] Midi G. On dense granular flows. Eur Phys J E . 2004;14:341–65. https://doi.org/10.1140/epje/i2003-10153-0.
[43] Mollon G, Zhao J. Fourier–Voronoi-based generation of realistic samples for discrete modelling of granular materials. Granul Matter . 2012;14:621–38. https://doi.org/10.1007/s10035-012-0356-x.
[44] Gadelmawla ES, Koura MM, Maksoud TMA, Elewa IM, Soliman HH. Roughness parameters. J Mater Process Technol 2002;123(1):133–45. https://doi.org/10.1016/S0924-0136(02)00060-2.
[45] Sandeep CS, Senetakis K. Computers and geotechnics an experimental investigation of the microslip displacement of geological materials. Comput Geotech 2019;107 (November 2018):55–67. https://doi.org/10.1016/j.compgeo.2018.11.013.
[46] Hillerborg A, Modéer M, Petersson P-E. Analysis of crack formation and crack growth in concrete by means of fracture mechanics and finite elements. Cem Concr Res 1976;6(6):773–81. https://doi.org/10.1016/0008-8846(76)90007-7.
[47] Barenblatt GI. The formation of equilibrium cracks during brittle fracture. General ideas and hypotheses. Axially-symmetric cracks. J Appl Math Mech 1959;23(3): 622–36. https://doi.org/10.1016/0021-8928(59)90157-1.
[48] Dugdale DS. Yielding of steel sheets containing slits. J Mech Phys Solids 1960;8(2): 100–4. https://doi.org/10.1016/0022-5096(60)90013-2.
[49] Zhou F, Molinari JF, Shioya T. A rate-dependent cohesive model for simulating dynamic crack propagation in brittle materials. Eng Fract Mech 2005;72(9): 1383–410. https://doi.org/10.1016/j.engfracmech.2004.10.011.
[50] Champagne M, Renouf M, Berthier Y. Modeling wear for heterogeneous bi-phasic materials using discrete elements approach. J Tribol 1603;136:02. https://doi.org/10.1115/1.4026053.
[51] Raje N, Sadeghi F. Statistical numerical modelling of sub-surface initiated spalling in bearing contacts. Proc Inst Mech Eng Part J J Eng Tribol 2009;223(6):849–58. https://doi.org/10.1243/13506501JET481.
[52] Jimenez S, Duddu R. On the parametric sensitivity of cohesive zone models for high-cycle fatigue delamination of composites. Int J Solids Struct 2016;82:111–24. https://doi.org/10.1016/j.ijsolstr.2015.10.015.
[53] Wang YJ, Ru CQ. Determination of two key parameters of a cohesive zone model for pipeline steels based on uniaxial stress-strain curve. Eng Fract Mech 2016;163: 55–65. https://doi.org/10.1016/j.engfracmech.2016.06.017.
[54] Ferracin T, Landis CM, Delannay F, Pardoen T. On the determination of the cohesive zone properties of an adhesive layer from the analysis of the wedge-peel test. Int J Solids Struct 2003;40(11):2889–904. https://doi.org/10.1016/S0020-7683(03)00076-3.
[55] Milanese E, Brink T, Aghababaei R, Molinari JF. Role of interfacial adhesion on minimum wear particle size and roughness evolution. Phys Rev E 2020;102(4): 1–12. https://doi.org/10.1103/PhysRevE.102.043001.
[56] Yuan CQ, Peng Z, Yan XP, Zhou XC. Surface roughness evolutions in sliding wear process. Wear 2008;265(3–4):341–8. https://doi.org/10.1016/j.wear.2007.11.002.
[57] Pham-Ba S, Molinari JF. Creation and evolution of roughness on silica under unlubricated wear. Wear 2021;472–473(Md). https://doi.org/10.1016/j.wear.2021.203648.